scientific reports

OPEN

Power quality improvement and energy management in hybrid microgrids using a dual-optimization approach

S. Joshua Daniel[1]✉, M. Karpagam[2], Aymen Flah[3,4,5]✉ & Slim Ben Chaabane[6]

Energy Management (EM) in hybrid Microgrids (MGs) is essential for coordinating Renewable Energy Sources (RESs) and Hybrid Energy Storage Systems (HESSs) to ensure Power Quality (PQ), stable operation, and efficient power flow. Existing optimization–prediction approaches often address these issues in isolation or require high computational overhead, limiting their real-time applicability. To overcome these challenges, this paper proposes a novel dual-optimization framework combining the Artificial Lemming Algorithm (ALA) with the Temporal Kolmogorov–Arnold Network (TKAN), referred to as ALA-TKAN. Unlike conventional methods, ALA-TKAN integrates metaheuristic-based optimization of power flow and HESS scheduling with sequence-aware forecasting of load and renewable generation, enabling proactive and coordinated EM under dynamic conditions. Implemented in MATLAB, the proposed method demonstrates superior performance compared with state-of-the-art techniques such as PDO-MACNN, BWO, PSO, ANN, and MRA-FLC, achieving minimal power loss (2.9 MW), highest efficiency (99.2%), lowest energy cost (0.8 $/Wh), and reduced THD (1.4%). These results confirm the novelty and practical potential of ALA-TKAN as a unified, computationally efficient strategy for PQ enhancement and reliable operation of hybrid MGs.

Keywords Diesel generator, Energy management, Hybrid energy storage system, Microgrid, Photovoltaic, Power quality, Proton exchange membrane fuel cell, Wind turbine

Background

The growing demand for clean and sustainable energy has led to the increased integration of RESs such as wind and solar into modern power systems[1]. These are ecologically friendly sources and they aid in the reduction of reliance on fossil fuels thus leading to reduced greenhouse gases emissions[2]. The diversity and intermittency of the RESs however usually renders fluctuations in power that can threaten PQ and grid stability. In order to curb these impacts and have a secure supply of power, an alternative viable option is the use of hybrid MGs, which integrates RESs and Energy Storage Systems (ESSs)[3,4]. The most frequently used energy imbalance control is instigated by the HESS, which basically consists of battery ESS and Fuel Cells (FCs) among other storage-supporting technologies[5]. Although battery ESS units have favorable opportunity in storing excess supply and providing long periods of supply, FCs have constant output power and have the properties to supplement the system at prolonged times of low output of production[6,7]. Battery ESS and FC combination increases flexibility and responsiveness of MG operations that leads to stability of voltages and frequency[8]. Proper integration of RESs and HESS contribute towards mitigation of PQ issues which include fluctuations in voltages and loads as well as deviations of frequency[9,10]. EM is found to be vital in the control of power flow between generation units, energy storage entities, and the loads that are connected in the system of hybrid MGs. These plans offer to make sure that energy resources at hand are used efficiently and that the system is also reliable[11]. EM facilitates the more stable delivery of power with its allocation of load reliefs and intermittence of generation. It also allows smooth switching between grid and island modes in case of disturbance[12,13]. PQ standards can also be sustained in

[1]Department of Electrical and Electronics Engineering, Hindusthan College of Engineering and Technology, Coimbatore, Tamil Nadu, India. [2]Department of Electrical and Electronics Engineering, Dhanalakshmi Srinivasan College of Engineering, Coimbatore, Tamil Nadu, India. [3]Applied Science Research Center, Applied Science Private University, Amman 11931, Jordan. [4]ENET Centre, CEET, VSB-Technical University of Ostrava, Ostrava, Czech Republic. [5]University of Business and Technology (UBT), Jeddah, Saudi Arabia. [6]Computer Engineering Department, Faculty of Computers and Information Technology, University of Tabuk, 47711 Tabuk, Saudi Arabia. ✉email: sjoshuadaniel.eee@gmail.com; aymen.flah@enig.u-gabes.tn

different operational situations with correct energy scheduling and load prioritization. The synergy of RESs, and HESS, especially through FC integration, contributes toward reducing interruptions and can enhance long-term energy viability[14]. Therefore, hybrid MGs with coordinated RES and FC-based HESS present an opportunity of developing a stable and efficient power distribution network[15].

Recent research reinforces these perspectives by advancing optimization and control strategies. For instance, GTOA-ACNN has been employed for energy hub management with RES integration, while CMBO-PCSANN-based PI controller tuning has been applied to PV-fed grids for PQ improvement[16,17]. Other studies have explored multiple MGs with EV charging under a GJO-PCGAN framework, hybrid wind–pumped hydro–CAES–fuel cell configurations for techno-economic evaluation, and EV performance enhancement through buck–boost converter integration[18–20]. Additionally, graph- and neural-based methods have been proposed for PQ enhancement and voltage regulation in DC MGs and distribution systems, while reconfigurable PV–wind MGs have been optimized for dispatch strategies[21–24]. Collectively, these advancements demonstrate that hybrid optimization and intelligent control significantly enhance reliability, PQ, and sustainability in renewable-based power systems.

Literature survey

Various studies have explored energy management (EM) strategies for power quality (PQ) improvement in microgrids (MGs) with renewable energy sources (RES) and hybrid energy storage systems (HESS), employing diverse technological approaches. This section reviews key contributions in this area. A study[25] proposed a hybrid PDO-MACNN algorithm for grid-free HRES power management in a HESS. In this method, the three-phase inverter controller parameters were optimized using PDO, while MACNN was employed to capture multi-scale temporal and spatial data. The approach minimized total harmonic distortion (THD), balanced active power between generation and load, and maintained the DC-link voltage within predefined limits through regulated charging and discharging. An EM power distribution strategy for a DC MG integrating photovoltaic (PV) arrays, proton exchange membrane fuel cells (PEMFC), lithium-ion batteries, and supercapacitors (SC) was presented in[26]. This method was based on the Black Widow Optimization (BWO) algorithm combined with the Equivalent Consumption Minimization Strategy (ECMS). The scheme not only enhanced system efficiency and reduced hydrogen consumption but also ensured equitable energy sharing among the components.

A PSO-based approach[27] was introduced for improving the performance of a HESS consisting of batteries, SCs, hydrogen fuel cells, and PV systems. By optimizing the parameters of a proportional-integral (PI) controller, the technique effectively regulated fuel flow rates, hydrogen utilization, and system stability, ensuring coordinated operation of all HESS elements. ANN-based EM[28] was investigated in DC MGs with HESS comprising batteries and SCs connected via a bidirectional converter. The ANN controller enabled optimal load distribution, maintained balanced state of charge (SoC) levels, and stabilized the voltage profile under variable PV generation conditions, while allowing dynamic energy exchange. A hybrid control strategy combining ANN and PI controllers[29] was explored for a DC MG integrating fuel cells, batteries, and SCs. This method maintained DC bus voltage stability, improved dynamic response, reduced battery stress, and extended the lifecycle of storage elements by enabling synchronized HESS operation under varying load demands.

A hybrid MRA-FLC approach[30] was proposed for EM in DC MGs supporting electric vehicle (EV) charging. The method ensured sustainable energy supply, minimized emissions, and protected storage devices against premature degradation by balancing power output between RESs and battery storage, ultimately enhancing resource efficiency, environmental sustainability, and system reliability. An intelligent EM system[31] was designed using a NARMA-L2 ANN model for MGs integrating PV, wind, and HESS with batteries and SCs. The system incorporated MPPT for PV based on NARX, and power allocation considered load demand, renewable output, and battery SoC. This approach reduced stress on batteries, ensured balanced energy allocation, and stabilized the DC bus voltage.

A PV-HESS MG stabilization system[32] was developed with a lead-acid battery and SC combination. A PI controller, optimized using three metaheuristic algorithms—Wild Horse Optimizer (WHO), Artificial Ecosystem-Based Optimization (AEO), and PSO—was applied to regulate the DC bus voltage. An EM strategy coordinated power flow among storage devices and managed MG connectivity, ensuring reliable operation across different load and generation scenarios. A comparative analysis of EM techniques for PQ improvement in MGs integrated with RES and HESS is presented in Table 1. Recently, advanced hybrid optimization–AI methods have also been explored for microgrid energy management. Reinforcement learning (RL)-based controllers can adaptively learn scheduling strategies under uncertain renewable and load conditions, improving resilience in real time. Similarly, physics-informed neural networks (PINNs) integrate system physics into neural architectures, enabling faster convergence and improved generalization in dynamic microgrid scenarios. These techniques offer promising results; however, they often demand high computational resources and large-scale training data, which can limit their deployment in real-time microgrid control.

Research gap and motivation

Despite these advances, there remains a lack of comprehensive EM strategies that holistically minimize power loss, reduce THD, lower energy cost, and improve conversion efficiency, while simultaneously ensuring voltage and frequency stability under dynamic operating conditions. Existing methods often lack the integration of forecasting with optimization, resulting in suboptimal or delayed responses to rapid system changes. To address this gap, this work proposes a novel dual-optimization EM framework that integrates the Artificial Lemming Algorithm (ALA) for optimized power flow and HESS scheduling with the Temporal Kolmogorov–Arnold Network (TKAN) for predictive load and renewable generation forecasting. This unified optimization–forecasting approach enables proactive scheduling, enhanced PQ, and improved system reliability in hybrid MGs.

Ref	Method	Scope	Reported performance	Limitations
[25]	PDO-MACNN	Grid-independent HRES with PV–HESS; DC-link regulation, THD minimization	THD reduced to 2.8%, DC-link voltage deviation < ± 3%	No forecasting; ignores energy pricing
[26]	BWO–ECMS	PV–PEMFC–Battery–SC DC MG; hydrogen efficiency	Efficiency 97.1%, hydrogen use reduced by 12%	Limited handling of dynamic load variation, storage degradation
[27]	PSO–PI	PV–Battery–SC–FC HESS; hydrogen minimization	Efficiency 96.5%, hydrogen savings ~ 10%, power loss ~ 4.8 MW	Slower adaptation under PV fluctuation; no future load modeling
[28]	ANN	PV-fed DC MG with Battery + SC; SoC balancing	Efficiency 95.9%, SoC maintained within 20–80%, THD ~ 3.5%	Lacks adaptive control for rapid changes
[29]	ANN + PI	DC MG with FC + HESS (Battery + SC); dynamic response	Bus voltage stability within ± 5%, efficiency 96.8%	No demand forecasting; limited fault handling
[30]	MRA–FLC	RES-based DC MG with EV charging	Efficiency 97.6%, THD ~ 2.9%, cost reduction ~ 8%	No long-term sustainability metrics
[31]	NARMA-L2 ANN + NARX MPPT	PV–Wind–HESS with Battery + SC; adaptive allocation	DC bus stable at ± 2%, THD ~ 3.1%	Limited adaptability to multi-timescale variations
[32]	WHO, AEO, PSO	PV–HESS with Battery + SC; voltage regulation	Efficiency ~ 97.2%, THD ~ 2.6%	Higher computational burden; scalability untested

Table 1. Comparative analysis of EM techniques for PQ improvement in MGs integrated with RES and HESS.

Contribution

The main contributions of this manuscript are summarized below,

J.S and A.F: Conceptualization, Methodology, Software, Investigation, Data Validation and Writing—Original draft preparation; K.M and S.C: Supervision, Resources, Data Validation, Visualization, Data Curation, Writing—Reviewing and Editing.

- Proposed a novel ALA-TKAN energy management method combining Artificial Lemming Algorithm (ALA) and Temporal Kolmogorov-Arnold Network (TKAN) for hybrid microgrids.
- Enhanced coordination of RES and HESS through ALA-based optimization of power flow distribution and energy storage control.
- Implemented predictive capability using TKAN to forecast power demand and renewable generation patterns for proactive energy management.
- Validated the proposed method against existing techniques (PDO-MACNN, BWO, PSO, ANN, MRA-FLC), demonstrating superior performance in power quality, stability, and reliability.

Novelty

The novelty of this work lies in the development of the ALA-TKAN technique for effective EM in hybrid MG systems integrated with RESs and HESS. The suggested approach integrates the optimization potential of the ALA with the temporal prediction power of the TKAN to develop a synchronized framework of scheduling and forecasting. The use of ALA aims at maximizing the flow of power and the recharging-discharging process of HESS components to achieve minimize power loss, energy cost, and THD and improve the coordination of the system and the voltage stability and frequency stability. At the same time, TKAN allows power demand and renewable generation forecasting, integrating the temporal dependence and non-linearity in system behaviors to enable more timely and knowledgeable control interventions. The integrated ALA-TKAN framework improves energy conversion efficiency, strengthens renewable integration, and ensures reliable EM under dynamic operating conditions, thereby contributing to the stable and sustainable operation of hybrid MGs.

Organization

The remaining of the paper is structured as follows: configuration of hybrid microgrid system integrated with RESs and HESS is explained in part 2. Part 3 describes the power quality enhancement in MG integrated with RESs and HESS based on ALA-TKAN technique. Part 4 explains results and discussion. Part 5 describes the conclusion.

Configuration of hybrid microgrid system integrated with RESs and HESS

Figure 1 illustrates the structure of a hybrid MG system integrated with RESs and a HESS. The system comprises Wind Turbines (WT) and PV panels connected to a DC bus through appropriate AC to DC and DC to DC converters, respectively. The FC and battery-based HESS are also interfaced to the DC bus via DC to DC converters, providing energy buffering and storage support. A Diesel Generator (DG) is connected through an AC to DC converter to supply additional power when needed. The Interlinking Converter (IC) manages power exchange between the DC and AC buses, regulated by the suggested ALA-TKAN-based energy management strategy. The AC bus delivers power to the grid and local loads, ensuring coordinated operation, efficient energy flow, and system stability under varying generation and demand conditions. The interlinking converter (IC) serves as the bidirectional interface between the DC and AC buses, regulating power exchange and maintaining DC-link voltage stability. The IC is governed by a PI-based current control strategy, where the active and reactive power references are generated according to system demand. To enhance adaptability, the reference signals of the IC are dynamically adjusted by the ALA-TKAN framework: ALA optimizes power-sharing among RES, HESS, and DG, while TKAN forecasts load and renewable generation trends to update the reference values

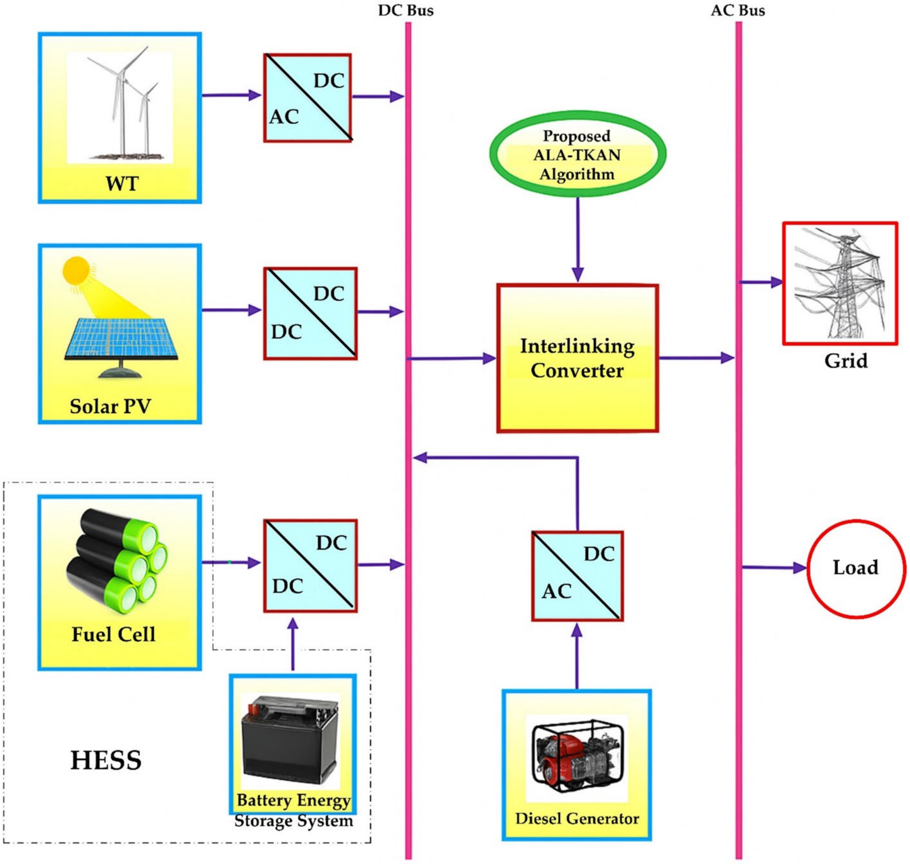

Fig. 1. Structure of hybrid MG system integrated with RESs and HESS.

proactively. This integrated strategy enables the IC to ensure seamless AC/DC coordination, stable operation, and effective support during grid-connected as well as islanded conditions.

PV modelling

Solar PV energy has emerged as one of the most common RESs during current times. The PV cell functions as an electric current generator which functions like a switched current source using a diode's operation[33]. A p–n junction forms the diode. Two series and parallel intrinsic resistors r_{is} and r_{ip}, have been incorporated into the model in order to study the physical processes at the cell level.

Consequently, Eqs. (1–3) can be used to model the solar cell in terms of the photocurrent i_{PH}, the current i_D through the diode, and the leakage current i_{SH}. Additionally, a cell's electrical properties are a little different from a diode's. Consequently, the Shockley Eqn is used to represent i_D, as illustrated below:

$$i_D = i_{SC}\left[EXP\left(\frac{v_{Photovoltaic} + r_s i_{Photovoltaic}}{nv_{Th}}\right) - 1\right] \tag{1}$$

where, n denotes ideality factor of diode which is between 1 and 2, r_s denotes intrinsic series resistance of cell, i_{SC} denotes diode's saturation current.

The following is the leakage current i_{SH} that the parallel resistance r_p causes:

$$i_{SH} = \frac{v_{Photovoltaic} + r_s i_{Photovoltaic}}{r_p} \tag{2}$$

where, r_p denotes cell intrinsic parallel resistance.

The cell's net current $i_{Photovoltaic}$ can be expressed as follows:

$$i_{Photovoltaic} = i_{PH} - i_D - i_{SH} \tag{3}$$

where, i_{PH} denotes photocurrent in shunt.

Therefore, the above governing Eqn can be expressed as follows by substituting i_D for i_{PH} and using their expressions:

$$i_{Photovoltaic} = i_{PH} - i_{SC}\left[EXP\left(\frac{v_{Photovoltaic} + r_s i_{Photovoltaic}}{n v_{Th}}\right) - 1\right] - \frac{v_{ip} + r_s i_{Photovoltaic}}{r_p} \tag{4}$$

With

$$v_{Th} = \frac{KT}{Q} \tag{5}$$

where, Q indicates electron charge, K indicates Boltzmann constant, T indicates temperature of the junction during its operation.

A collection of basic PV cells coupled in parallel or series makes up a PV generator. Consequently, the current supplied by the PV panel as a function of the number of cells in series N_s and parallel N_p is described by the following Eq. (6):

$$\begin{aligned} i_{Photovoltaic} = N_p i_{Photovoltaic} - N_p i_{SC}\left[EXP\left(\frac{v_{Photovoltaic} + r_s i_{Photovoltaic}}{nKTN_s}\right) - 1\right] \\ -N_p Q\left(\frac{v_{Photovoltaic} + r_s i_{Photovoltaic}}{N_s r_p}\right) \end{aligned} \tag{6}$$

WT modelling

The wind's kinetic energy is converted by the WT into rotational energy in the form of a torque[34]. Equation (7) provides the power available in the wind.

$$p_V = \frac{1}{2}\rho a v^3 \tag{7}$$

where, $a = \pi r^2$ indicates area swept by turbine blades, ρ denotes air density, v indicates wind speed.

Equation (8) provides the power that the turbine draws from the wind's available power.

$$p_T = \frac{1}{2}\rho\pi r^2 v^3 c_P\left(\lambda, \beta\right) \tag{8}$$

where, r denotes radius of turbine rotor, $c_P\left(\lambda, \beta\right)$ denotes power coefficient, c_P denotes function of tip speed ratio (λ) and the pitch angle (β).

The λ is expressed in Eq. (9)

$$\lambda = \frac{r\omega_T}{v_V} \tag{9}$$

where, ω_T denotes angular rotational speed of WT rotor.

Modelling of DG

A mechanical actuator system and a proportional speed control are the two components of the DG model[35]. The diesel engine's dynamic model can be written as follows:

$$\begin{cases} \dot{Q}_1 = Q_2 \\ \dot{Q}_2 = {}^{1}/_{t_2 t_3} Q_1 - {}^{t_2 + t_3}/_{t_2 t_3} Q_2 + p_{ref} + M\left(\omega_{ref} - \omega\right) \end{cases} \tag{10}$$

$$p_M = {}^{1}/_{t_2 t_3} Q_1 + {}^{t_1}/_{t_2 t_3} Q_2 \tag{11}$$

where, Q_1 and Q_2 are the state variables in the controllable canonical form of the DG, p_M denotes mechanical power, ω denotes rotor speed, ω_{ref} denotes speed reference, t_1, t_2, t_3 denotes DG time constants, M denotes speed droop gain, p_{ref} denotes power reference.

Modelling of PEMFC

By converting chemical energy into electrical power, the FC generates electricity using the same mechanism as batteries[36]. Simply by oxidizing hydrogen without the need for a mechanical handle. The chemical reaction outlined in Eq. (12) produces the PEM FC's output voltage.

$$O_2 + 2H_2O + \to heat + energy \tag{12}$$

By assuming all losses that resulted in voltage dips in a PEMFC, the Eq. (13) below can be utilized to express the PEMFC voltage stack in current terms.

$$N v_{Fuel\ cell} + N\left(e_{NERST} + v_{ACT} + v_{OHMIC} + v_{CON}\right) \tag{13}$$

where, N denotes cell number, e_{NERST} refers reversible voltage, v_{ACT} refers activation losses, v_{OHMIC} refers ohmic losses, v_{CON} refers losses of concentration.

$$e_{NERST} = 1.229 - \left[\left(\frac{RT}{sF} \right) In \left(\frac{p_{H_2O}}{p_{H_2} * \sqrt{p_{O_2}}} \right) \right] \tag{14}$$

where, R indicates universal gas constant, T refers temperature of cell, s denotes count of transferred electrons and F refers Faraday constant, p_{H_2} and p_{O_2} are the H_2 and O_2 pressures respectively.

$$v_{ACT} = \xi_1 + \xi_2 T + \xi_3 T \; Inc_{O_2} + \xi_4 T \; Ini_{Fuel\ cell} \tag{15}$$

where, ξ_1 = Constant term for concentration loss.
ξ_2 = Current density coefficient.
ξ_3 = Oxygen concentration coefficient.
ξ_4 = temperature coefficient, i refers current of FC, c_{O_2} refers concentration of $O_{2.}$

$$v_{OHMIC} = -i_{Fuel\ cell} r_m \tag{16}$$

where, r_m refers membrane resistance.

$$r_m = \frac{\rho_m L_m}{a} \tag{17}$$

where, cell active area a, membrane thickness L_m, and membrane sensitivity ρ_M.

$$v_{CON} = b \left(1 - \frac{i_{Fuel\ cell}}{i_{L_{Max}} A} \right) \tag{18}$$

where, i_{Max} denotes the maximum current density, A refers to a constant.

Modelling of battery ESS

The BESS's charging and discharging process is shown in Eq. (19)[37].

$$electricity_{BESS}(T) = electricity_{BESS}(t-1) \times (1-\sigma) + \begin{bmatrix} p_{Ch\arg e}(T) \times \eta_{Ch\arg e} \times \mu_1(T) - p_{Disch\arg e}(T) / \eta_{Disch\arg e} \\ \times \mu_2(T) \end{bmatrix} \times \Delta T \tag{19}$$

where, σ $_{\text{indicates}}$ self-discharge rate, $electricity_{BESS}(T)$ denotes electricity in BESS at time T, $p_{Ch\arg e}(T)$ denotes charging power at time T, $\eta_{Ch\arg e}$ indicates efficiency of charging, $p_{Disch\arg e}$ denotes discharging power at time T, $\eta_{Disch\arg e}$ denotes efficiency of discharging, ΔT indicates time interval. The following limitations must also be followed by BESS.

$$\mu_1(T) + \mu_2(T) = [0, 1] \tag{20}$$

$$\mu_1(T) = [0, 1] \tag{21}$$

$$\mu_2(T) = [0, 1] \tag{22}$$

These restrictions prevent BESS from always being charged as well as discharged simultaneously. In Eq. (20), the BESS's charging and discharging states are denoted by the letters $\mu_1(T)$ and $\mu_2(T)$. The BESS is charging or discharging if the number is 1, and the opposite is true if the number is 0.

Objective function

To determine the THD use the following Eq. (23):

$$THD = \frac{\sqrt{\sum_{n=2}^{\infty} X_n^2}}{X_1} \times 100\% \tag{23}$$

where, RMS value of the n $^{\text{th}}$ harmonic component is shown by X_n, while the RMS value of the fundamental component (voltage or current) is indicated by X_1.

Power quality enhancement in MG integrated with RESs and HESS based on ALA-TKAN technique

Minimization of power loss, THD, and energy cost, along with the enhancement of energy conversion efficiency and the maintenance of voltage and frequency stability in hybrid MG systems integrating RESs and HESS, is suggested in this paper. The technique optimizes power flow and HESS control through the adjustment of energy management parameters, while accurately predicting renewable generation and power demand patterns to support proactive decision-making. The subsequent is a detailed description of the ALA-TKAN technique and its implementation for improved performance in RES-HESS-based hybrid MG systems.

Optimization using ALA technique

The ALA is a novel bio-inspired meta-heuristic that simulates four natural behaviors of lemming's long-distance migration, digging holes, foraging, and evading predators to guide the search for optimal solutions[38]. These behaviors are mathematically modeled to ensure a strong balance between exploration and exploitation during the search process. ALA integrates Brownian motion and Levy flight to enhance its ability to escape local optima and improve global search efficiency. It also features an energy-decreasing mechanism that adaptively shifts focus from broad exploration in the early stages to focused exploitation later. While several recent metaheuristic algorithms such as Harris Hawks Optimization (HHO), Slime Mould Algorithm (SMA), and Whale Optimization Algorithm (WOA) have been reported for energy optimization tasks, the Artificial Lemming Algorithm (ALA) was selected in this study owing to its superior balance between exploration and exploitation, adaptive energy-decreasing mechanism, and reduced computational complexity. The four natural behaviors modeled in ALA (migration, digging, foraging, and predator evasion) enable both global and local search capabilities, while Brownian motion and Lévy flight enhance its ability to escape local minima. These features allow ALA to converge more rapidly and reliably than HHO, SMA, or WOA, particularly under multi-objective conditions involving simultaneous minimization of power loss, THD, and energy cost, alongside maximization of efficiency and stability. Additionally, ALA demonstrated shorter execution time and higher robustness in preliminary tests, making it more suitable for real-time energy management in hybrid microgrids.

Step 1: Initialization
To initialize the input parameters such as wind power, PV power, battery power, etc.

Step 2: Random generation
The input parameter in a matrix described by is generated at random.

$$\overrightarrow{Y} = \begin{bmatrix} y_{1,1} & y_{1,2} & \cdots & y_{1,\dim -1} & y_{1,\dim} \\ y_{2,1} & y_{2,2} & \cdots & y_{2,\dim -1} & y_{2,\dim} \\ \cdots & \cdots & y_{j,k} & \cdots & \cdots \\ \vdots & \vdots & \vdots & \vdots & \vdots \\ y_{n-1,1} & y_{n-1,2} & \cdots & y_{n-1,\dim -1} & y_{n-1,\dim} \\ y_{n,1} & y_{n,2} & \cdots & y_{n,\dim -1} & y_{n,\dim} \end{bmatrix} \tag{24}$$

where, the set of all initial candidate solutions $\overrightarrow{Y}$ denotes matrix consisting of n is population size, $\dim$ is number of dimensions between the upper and lower bounds.

Step 3: Fitness function
Evaluate the fitness value of each candidate solution based on criteria such as minimized THD of the system.

$$F = Min\,(THD) \tag{25}$$

where, F denotes fitness function.

Step 4: Exploration phase
When the energy factor is $E\,(T) > 1$, ALA enters the exploration phase. This state promotes wide search to identify promising operational strategies for power distribution and HESS scheduling. This phase is guided by two behaviors inspired by biology:

Long-distance migration This simulates the behavior of lemmings migrating long distances to find new energy coordination possibilities across MG components, preventing premature convergence and enabling identification of better configurations.

$$\vec{Y_j}\,(T+1) = \vec{Y}_{BEST}\,(T) + f \times \overrightarrow{BrM} \times \left(\vec{r} \times \left(\vec{Y}_{BEST}\,(T) - \vec{Y_j}\,(T)\right)\right) + (1-\vec{r}) \times \left(\vec{Y_j}\,(T) - \vec{Y_j}\,(T) - \vec{Y_b}\,(T)\right) \tag{26}$$

where, $\vec{Y_j}\,(T+1)$ denotes location of the j th search agent at $(T+1)$ iteration, $\vec{Y}_{BEST}\,(T)$ denotes current optimal solution, f denotes served as flag to change the search direction, $\overrightarrow{BrM}$ denotes vector of random numbers characterizing Brownian motion, $\vec{r}$ denotes vector size, $\vec{Y_j}\,(T)$ denotes current location of the j th search agent, $\vec{Y_b}\,(T)$ denotes randomly selected search individual from the population, b denotes an integer index between 1 and n.

Digging holes This reflects moderate-range exploration, where candidate solutions perform diversified searches around their current positions to discover sub-optimal HESS and power flow configurations.

$$\vec{Y_j}\,(T+1) = \vec{Y_j}\,(T) + f \times l \times \left(\vec{Y}_{BEST}\,(T) - \vec{Y_b}\,(T)\right) \tag{27}$$

$$l = Rand \times \left(1 + \sin\left(\frac{T}{2}\right)\right) \tag{28}$$

where, denotes random number related to the current number of iterations.

Step 5: Exploitation phase
When the energy is $E\,(T) \leq 1$, ALA enters the exploitation phase. The agents have now depleted their energy and shifted their attention from conducting a wide search to focusing more intently on regions that show

promise. The algorithm narrows its search to refine control strategies that show potential for optimal power flow and HESS coordination.

Foraging for food Lemming's propensity to forage for food in a restricted region close to their shelter serves as the model for this behavior. Agents conduct spiral-based localized searches around the current best-known solution to fine-tune the scheduling of energy sources and storage usage in the MG.

$$\vec{Y}_j\left(T+1\right)=\vec{Y}_{BEST}\left(T\right)+f\times spiral\times Rand\times\vec{Y}_j\left(T\right) \tag{29}$$

where, $spiral$ indicates spiral shape of the random search during foraging.

Evading predators This behavior, which was inspired by lemming's escape responses, enables agents to use Levy flight to make abrupt, large jumps in order to avoid possible local minima. This randomness aids in identifying alternate power flow routes and storage utilization schemes.

$$\vec{Y}_j\left(T+1\right)=\vec{Y}_{BEST}\left(T\right)+f\cdot g\cdot Levy\left(\dim\right)\times\left(\vec{Y}_{BEST}\left(T\right)-\vec{Y}_j\left(T\right)\right) \tag{30}$$

where, f denotes escape coefficient of lemming's, $Levy\left(\cdot\right)$ denotes levy flight function, employed to mimic the deceptive maneuvers of lemmings during escape.

Step 6: Updating

Each search agent updates its position by selecting an exploration or exploitation behavior based on the energy factor, continuously improving power flow strategies and HESS control variables in alignment with operational goals.

$$E\left(T\right)=4\times\arctan\left[1-\frac{T}{t_{MAX}}\right]\times\ln\left(\frac{1}{Rand}\right) \tag{31}$$

where, $E\left(T\right)$ denotes energy factor, t_{MAX} denotes maximum number of iterations.

Step 7: Termination

The method ends when the termination condition is satisfied, and the optimal solution discovered throughout the optimization process is given back as the output. If not, the algorithm iteratively refines the answers until one of the termination requirements is met, then goes back to step 3 and repeats the process. Flowchart of ALA is presented in Fig. 2.

Prediction using TKAN technique The TKAN is utilized to predict power demand and renewable generation patterns to support proactive energy management decisions, enhance power quality, and coordinate the operation of HESSs in hybrid microgrids with integrated RESs[38]. TKAN is designed to analyze sequential energy-related variables such as voltage, current, power flow, and generation trends to ensure stable power delivery and optimized operation. Built upon Recurrent Kolmogorov-Arnold Networks (RKANs) and based on the Kolmogorov-Arnold representation theorem, TKAN decomposes complex multivariable relationships into compositions of learnable univariate transformations. This decomposition supports the effective modeling of nonlinear patterns and uncertainties in electrical parameters. Each layer of TKAN incorporates memory-aware structures that retain previous operational conditions, enabling accurate forecasting of dynamic behaviors, including load fluctuations, renewable output variations, and disturbances affecting power quality.

Each TKAN layer retains historical sequence data through a memory-integrated recurrent structure, allowing it to track changes in power demand, PV power, and wind power, HESS power variability. The hidden state update at each time step is computed as:

$$H_T=F\left(w_{HH}H_{T-1}+w_{HY}Y_T+B_H\right) \tag{32}$$

where, H_T denotes hidden state at time T, Y_T denotes input vector, H_{T-1} denotes previous hidden state, w_{HH} and w_{HY} denotes learned weights, B_H denotes bias term, $F(\cdot)$ denotes nonlinear activation function.

The RKAN input at each layer and timestep is contextually constructed using past memory, enabling the network to learn sequence-aware embeddings as shown in Eq. (33):

$$S_{L,T}=w_{L,\tilde{Y}}Y_T+w_{L,\tilde{H}}\tilde{H}_{L,T-1} \tag{33}$$

where, $S_{L,T}$ denotes the input to RKAN layer L, $w_{L,\tilde{Y}}$ and $w_{L,\tilde{H}}$ denotes learned weights, $\tilde{H}_{L,T-1}$ denotes memory from the previous time step.

The memory state is updated by combining past memory and new KAN output in Eq. (34):

$$\tilde{H}_{L,T}=w_{HH}\tilde{H}_{L,T-1}+w_{HZ}\tilde{O}_T \tag{34}$$

where, $\tilde{H}_{L,T}$ denotes updated memory state, $\tilde{O}_T$ denotes current RKAN output, w_{HZ} denotes learnable weight matrix for the current output.

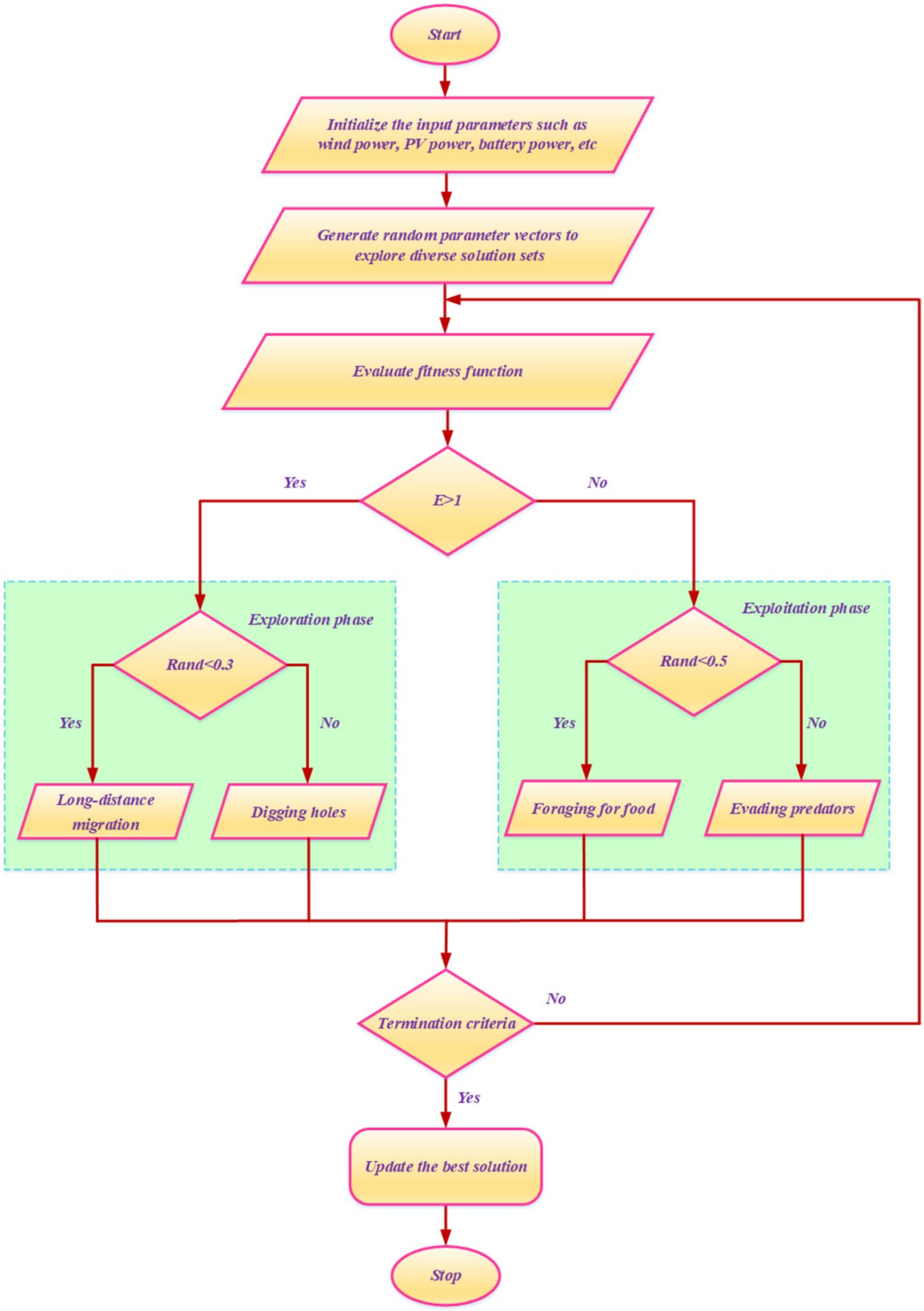

Fig. 2. Flowchart of ALA.

To further strengthen long-range temporal learning, a modified LSTM mechanism governs the internal memory transitions using forget and input gates, which are crucial for modeling load cycles and renewable intermittency:

$$C_T = F_T \Theta C_{T-1} + j_T \Theta \underset{T}{\overset{\leftharpoonup}{C}} \tag{35}$$

where, C_T denotes current memory state, F_T and j_T denotes forget and input gate activations, denotes candidate memory, Θ denotes element-wise multiplication.

The final prediction is made using the hidden state output, updated as:

$$H_T = O_T \Theta \tanh\left(C_T\right) \tag{36}$$

where, H_T denotes hidden state used for prediction at time T, O_T denotes output gate, C_T denotes cell state, $\tanh(\cdot)$ denotes nonlinearity for output modulation.

This forecasting framework enables TKAN to learn detailed sequence-aware representations and deliver accurate predictions of future power demand and renewable generation, thereby supporting improved energy scheduling, power quality, and HESS coordination control in hybrid MGs with high renewable integration.

For training and validation, the TKAN model was provided with 1,200 sequential samples representing PV generation, wind generation, and load demand patterns derived from the simulation environment. The dataset was sampled at a rate of 0.1 s to capture short-term fluctuations in renewable output and demand dynamics. Forecasting performance was evaluated using standard statistical error metrics: Root Mean Square Error (RMSE) and Mean Absolute Percentage Error (MAPE). The TKAN achieved an RMSE of 0.42 kW and a MAPE of 2.8%, confirming its ability to accurately forecast renewable generation and demand variations. These results validate the predictive reliability of TKAN and its role in supporting proactive energy management decisions within the ALA-TKAN framework.

Results and discussion

The performance of the suggested ALA-TKAN method for enhancing EM in hybrid MG systems integrated with RESs and HESS is demonstrated in this section through simulation results. This method aims to minimize power loss, THD, and energy cost, while improving energy conversion efficiency and maintaining voltage and frequency stability by optimizing power flow and HESS control, and accurately predicting renewable generation and power demand. The approach has been implemented on MATLAB, and its effectiveness in coordinating energy distribution and ensuring stable system operation under varying conditions has been thoroughly evaluated and compared with existing techniques. All simulations were executed in MATLAB/Simulink R2023a on a workstation with Intel® Core™ i7-10750H CPU @ 2.60 GHz, 16 GB RAM, and Windows 10 (64-bit). The reported execution times in Table 2 correspond to this environment, ensuring a consistent and fair basis for comparison across all tested methods. Table 2 provides a detailed simulation parameters used in the proposed system.

Figure 3 shows the wind power output. At the start, the power increases rapidly from 0 kW to a peak of about 15 kW at 0.2 s, reflecting a sudden change in wind speed or generator dynamics. After this transient peak, the output settles to a steady level of 10 kW from around 0.4 s onward and remains constant for the rest of the simulation. This stable performance indicates either consistent wind conditions or effective regulation by the control system following the initial transient.

Figure 4 presents the power output of the photovoltaic (PV) system. Initially, the output starts at 0 kW and rises sharply, reaching approximately 6 kW at around 0.2 s. This rapid increase corresponds to the system's immediate response to the applied irradiance. After the initial ramp-up, the PV output stabilizes and maintains

Component	Parameter	Value/assumption	Reference/remark
PV system	Rated capacity	6 kW	Based on simulation setup
	Irradiance level (G)	1000 W/m^2	Standard test condition
	Cell temperature	25 °C	STC
	Series resistance (Rs)	0.01 Ω	From[24]
	Parallel resistance (Rp)	100 Ω	From[24]
Wind turbine	Rated capacity	10 kW	Simulation setup
	Air density (ρ)	1.225 kg/m^3	At sea level
	Rotor radius (R)	2.5 m	Selected for simulation
	Cut-in/Rated/Cut-out speed	3 m/s/12 m/s/25 m/s	Typical small-scale WT
	Power coefficient (Cp,max)	0.42	From[25]
PEM fuel cell	Rated power	28 kW	Simulation setup
	H_2 input pressure	1.5 atm	Assumption
	O_2 input pressure	1 atm	Assumption
	Operating temperature	353 K (80 °C)	Typical PEMFC
	Number of cells (N)	50	Simulation
Diesel generator (DG)	Rated capacity	15 kW	Backup generator
	Speed droop gain	5%	From[26]
	Time constant	0.2 s	From[26]
Battery ESS	Capacity	20 kWh	Assumption
	Rated power	10 kW	Simulation
	Efficiency (ηc/ηd)	0.95/0.95	[28]
	SOC range	20–90%	Protection constraint
General simulation assumptions	Sampling time	0.001 s	MATLAB setup
	Simulation duration	6 s	For transient and steady state

Table 2. Simulation parameters and assumptions for RES and HESS models.

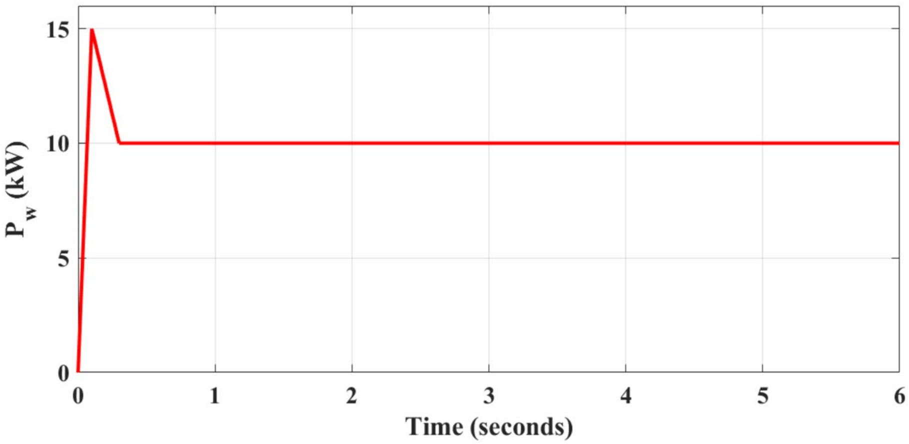

Fig. 3. Evaluation of wind power.

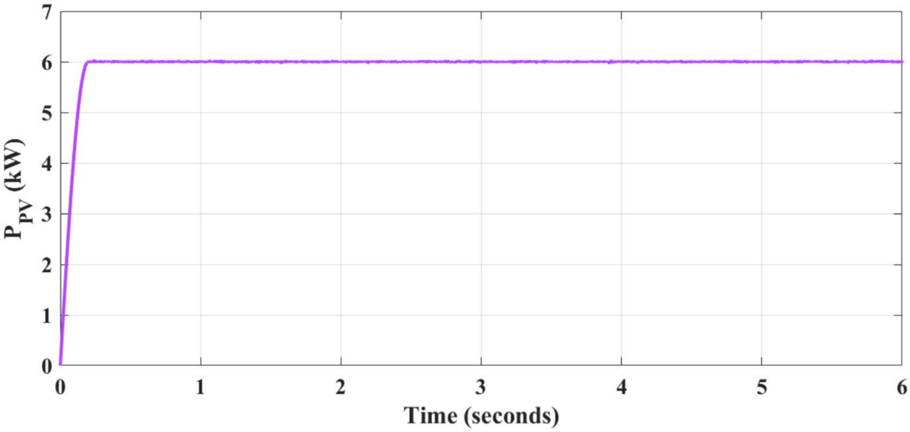

Fig. 4. Evaluation of PV Power.

a nearly constant value of 6 kW for the remainder of the simulation period. The negligible fluctuations observed during the steady-state phase indicate uniform solar irradiance and demonstrate the effectiveness of the PV system's control mechanism in sustaining a consistent power output despite minor dynamic variations.

Figure 5 illustrates the DC-link voltage profile. From the start of the simulation until approximately 5 s, the voltage remains stable at around 700 V, reflecting steady operation of the DC-link under nominal conditions. At 5 s, a step change occurs, causing the voltage to rise to about 720 V. This transition indicates a change in the system's operating conditions, likely due to variations in power input or load demand. Following this adjustment, the DC-link voltage quickly stabilizes at the new level of 720 V, demonstrating the effectiveness of the regulation and control mechanisms in maintaining stability under altered operating modes.

Figure 6 illustrates the battery power output. Initially, the battery discharges sharply, peaking at approximately 10 kW before rapidly dropping to near 0 kW around 0.2 s. Between the 0.2 s and 4 s the battery is in charging mode, with power switched slightly around the 4 kW. At 4 s, the mode shifts as the power drops to approximately −5 kW, indicating a transition to discharging. This discharging goes up to 5 s after which the battery goes back to a neutral or standby situation where power is at 0 kW. These transitions represent dynamic duty cycle capacity of the battery to respond to fluctuations in energy demand and generation conditions, which allow maintaining energy parity in the system.

Figure 7 illustrates the load demand profile over the simulation period. At the beginning, the load power quickly rises to approximately 25 kW and remains constant until about 1 s. Between 1 and 2.5 s, the demand decreases to 20 kW, representing a temporary reduction in load. At 2.5 s, the load recovers to 25 kW and sustains this level until 4 s. Beyond 4 s, the power demand decreases sharply to around 15 kW and stabilizes at this level for the remainder of the simulation. These discrete step changes in the load profile emulate realistic variations in consumption patterns, creating a dynamic operating environment that effectively tests the adaptability and responsiveness of the energy management (EM) system.

Figure 8 shows the IC power output. The power begins at 0 kW and rises quickly to approximately 3 kW, where it remains with minor fluctuations until around 1 s. Between 1 and 2.5 s, the power drops and fluctuates around 0 kW. At 2.5 s, there is a sharp spike reaching about 6 kW, followed by a return to a fluctuating level around 4 kW.

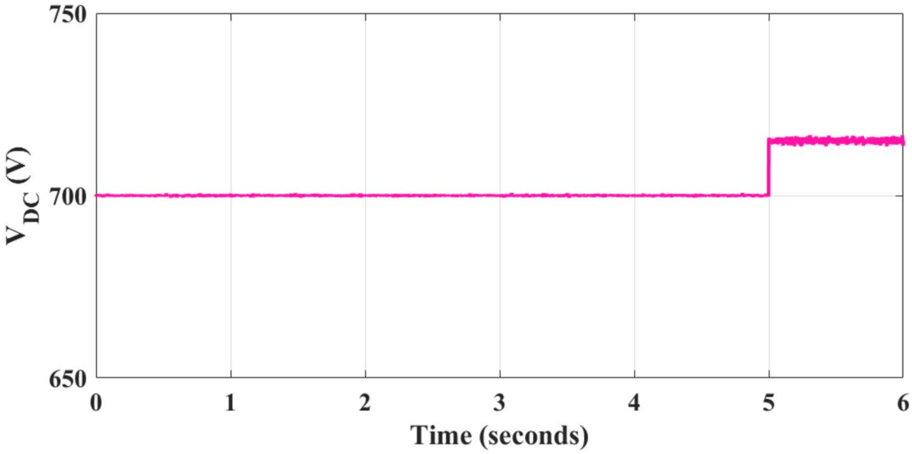

Fig. 5. Evaluation of DC-link voltage.

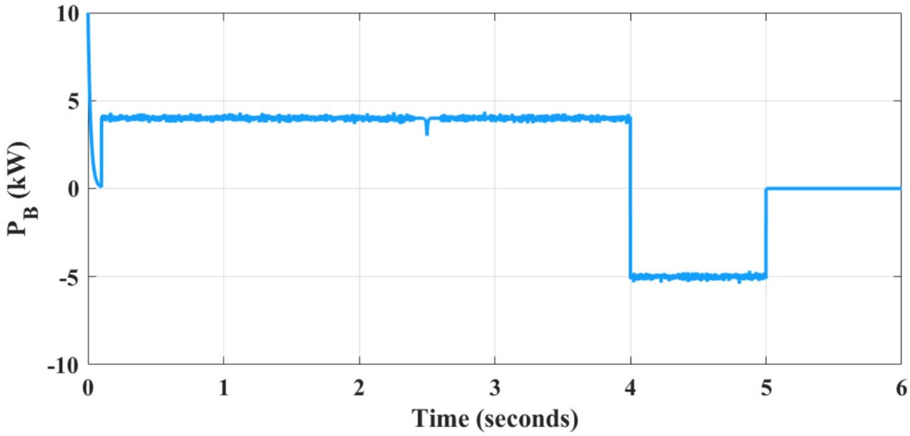

Fig. 6. Evaluation of battery power.

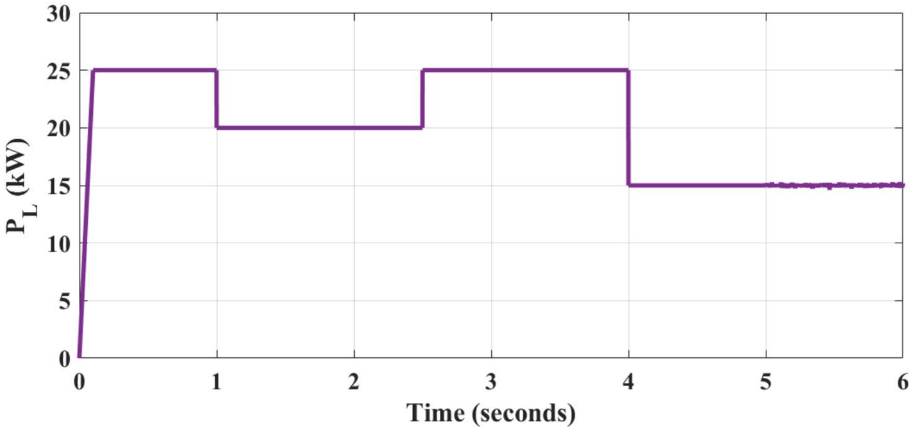

Fig. 7. Evaluation of load power.

This continues until 4 s, after which the power drops and stabilizes near 2 kW. At 5 s, the interlinking converter switches to a negative power flow of approximately −2 kW, indicating reverse power transfer, and remains at that level with slight variations. These dynamic changes demonstrate the interlinking converter's role in balancing power between subsystems during variations in generation and load conditions.

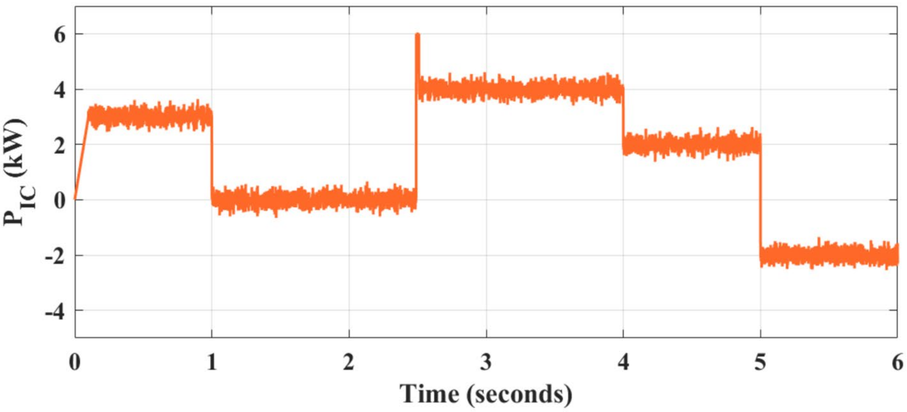

Fig. 8. Evaluation of IC power.

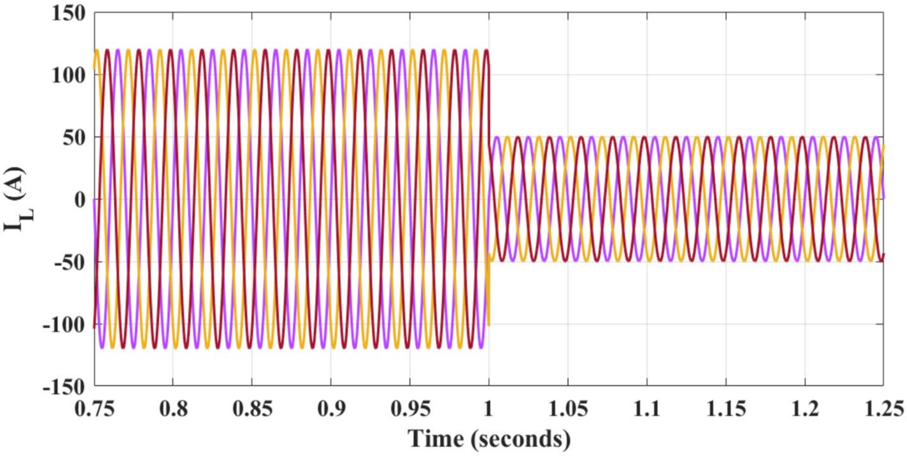

Fig. 9. Evaluation of load current.

Figure 9 depicts the load current waveform. Initially, the current has a peak amplitude of approximately ± 120 A and exhibits a stable sinusoidal pattern up to 1 s, representing operation under a higher load condition. At exactly 1 s, a sudden transition occurs, and the current amplitude decreases to about ± 50 A, indicating a reduction in load demand. Despite this change in magnitude, the waveform preserves its sinusoidal shape, frequency, and symmetry, demonstrating consistent and stable current behavior under both high- and low-load conditions.

Figure 10 shows the grid current. From 0.75 to 1 s, the current exhibits a balanced three-phase sinusoidal waveform with peak amplitudes of approximately ± 100 A, indicating active power exchange with the grid. At precisely 1 s, three-phase currents abruptly drop to zero, signifying complete disconnections from the grid. The waveform remains flat at 0 A beyond this point, confirming no current contribution from the grid after disconnection. Figure 11 illustrates the voltage of load. The voltage maintains consistent peak amplitude of approximately ± 325 V. Despite the disconnection from the grid at 1 s, there is no observable disturbance or drop in voltage, indicating seamless voltage support from local generation or storage units. The waveform remains stable and undistorted, ensuring reliable voltage supply to the load.

Figure 12 illustrates the three-phase grid voltage. Initially, the voltage exhibits a stable sinusoidal waveform with peak values oscillating around ± 325 V, reflecting normal grid operation. This condition persists until 1 s, at which point the voltage abruptly collapses to zero and remains flat throughout the interval from 1 to 1.25 s. Such a sudden drop indicates a grid disconnection or fault event, effectively captured by the system. This transition is crucial for evaluating the system's ability to detect and respond to grid disturbances, thereby ensuring stability and protection.

Figure 13 presents the grid power profile. From 0 to 1 second, the grid supplies a steady output of approximately 40 kW. At exactly 1 second, the power abruptly falls to nearly 0 kW and remains at this level until 2.5 seconds, signifying a temporary grid outage or a shift in the energy supply source. After 2.5 seconds, the grid power recovers to about 40 kW and stays stable up to 5 seconds. Beyond this point, the output decreases and stabilizes at around 30 kW between 5 and 6 seconds. These fluctuations reflect the system's adaptive capability in regulating energy exchange with the grid under varying operating conditions.

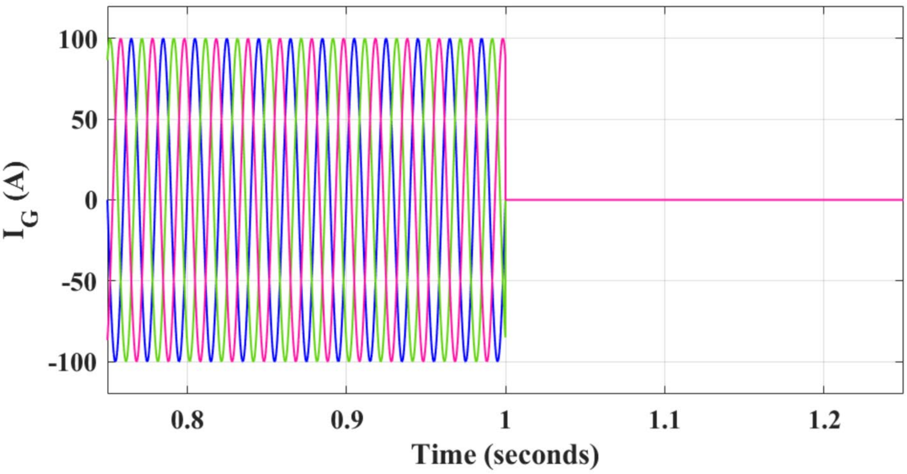

Fig. 10. Evaluation of grid current.

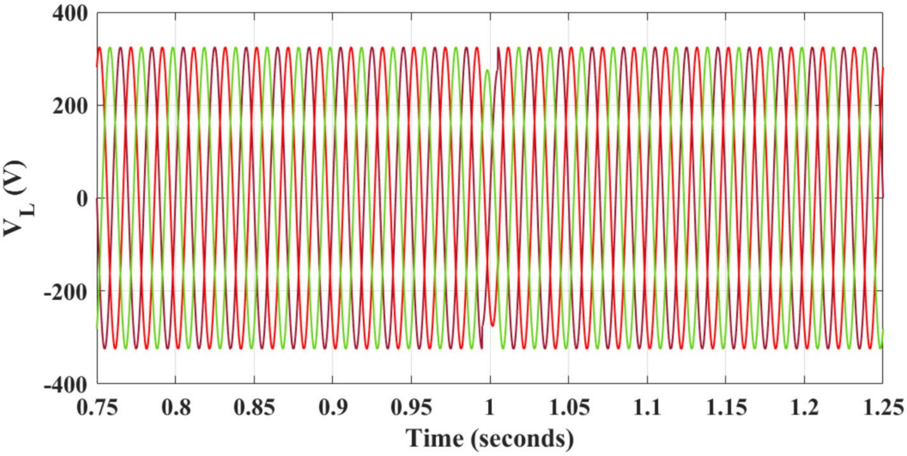

Fig. 11. Evaluation of load voltage.

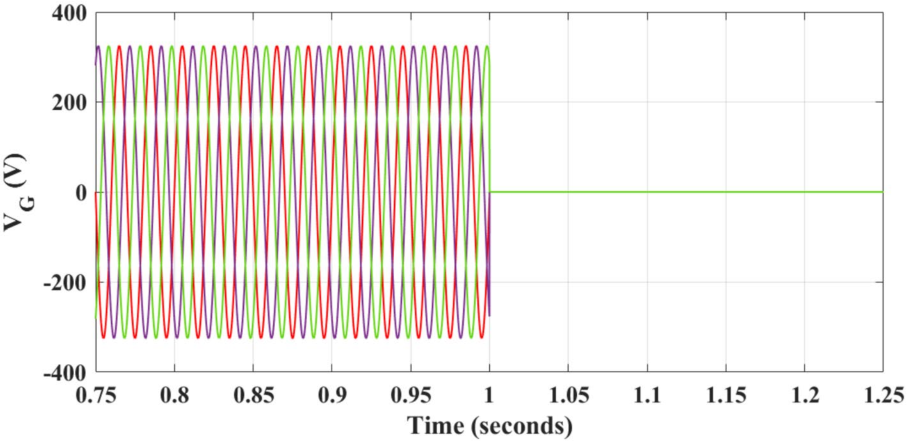

Fig. 12. Evaluation of grid voltage.

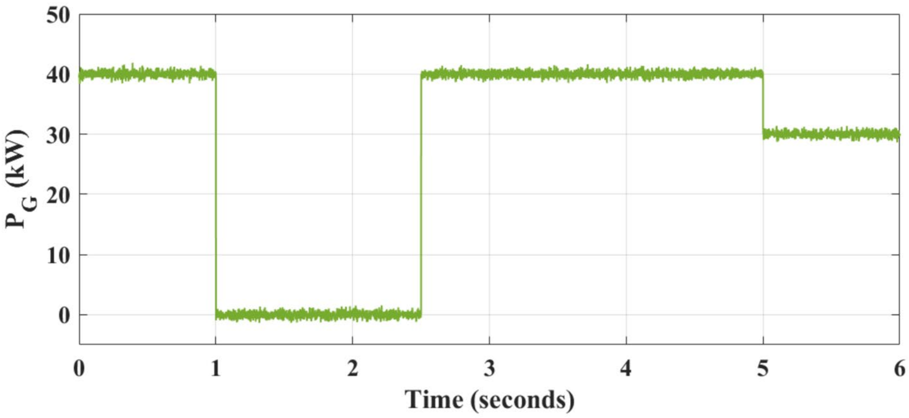

Fig. 13. Evaluation of grid power.

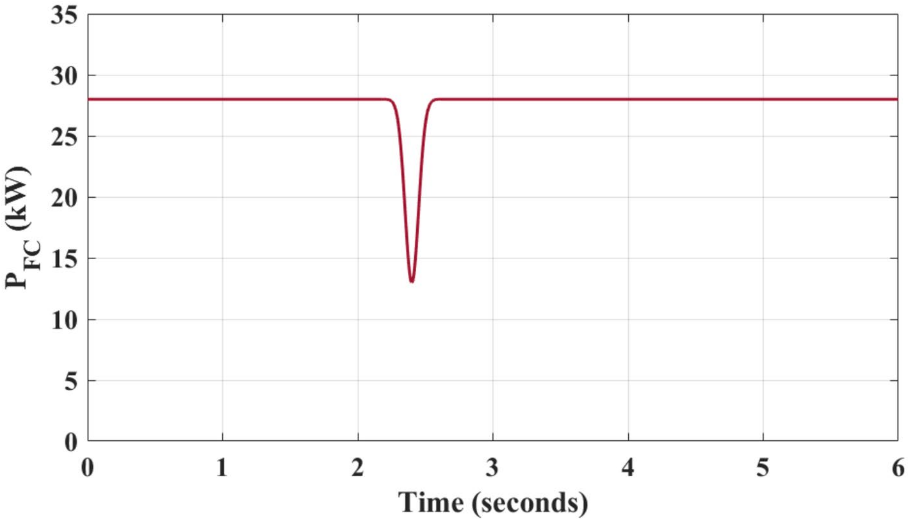

Fig. 14. Evaluation of fuel cell power.

Figure 14 shows the fuel cell (FC) power output. From the start of the simulation until approximately 2.2 s, the FC delivers a stable power of around 28 kW, reflecting steady operation under normal conditions. Between 2.2 and 2.6 s, a sharp dip occurs, with the power momentarily dropping to nearly 14 kW. This transient reduction suggests a temporary disturbance or adjustment in load-sharing dynamics. Following this event, the FC output quickly recovers and stabilizes back at 28 kW for the remainder of the simulation, demonstrating the system's robustness in managing transient conditions while maintaining steady-state performance. Figure 15 illustrates the diesel generator (DG) power output. From 0 to 1 s, the DG remains inactive at 0 kW. At 1 s, it starts operating, initially supplying approximately 10 kW. The output then gradually rises, peaking at around 14.5 kW just before the 3-s mark. At exactly 3 s, the DG is switched off, and its output drops back to 0 kW, where it remains for the rest of the simulation. This controlled activation and deactivation highlight the system's capability for dynamic dispatch of the generator, ensuring that power supply aligns with load demand or varying grid conditions.

Table 3 presents a detailed comparison between the proposed method and several existing approaches. The suggested method achieves the lowest power loss at 2.9 MW, compared to 3.4 MW for PDO-MACNN, 4.3 MW for BWO, 5.1 MW for PSO, 5.6 MW for ANN, and 4.0 MW for MRA-FLC. It also attains the highest efficiency of 99.2%, while other methods achieve 98.2% for PDO-MACNN, 97.3% for BWO, 96.4% for PSO, 95.7% for ANN, and 97.8% for MRA-FLC. The energy cost is minimized at 0.8 \$/Wh, in contrast to 1.1, 1.4, 1.5, 1.9, and 1.2 for PDO-MACNN, BWO, PSO, ANN, and MRA-FLC respectively. The suggested approach also demonstrates the shortest execution time of 19 s, outperforming others such as PDO-MACNN with 25 s, BWO with 31 s, PSO with 29 s, ANN with 35 s, and MRA-FLC with 22 s. In terms of total harmonic distortion, it records the lowest value at 1.4%, compared to 2.1% for PDO-MACNN, 3.4% for BWO, 2.9% for PSO, 3.8% for ANN, and 2.7% for MRA-FLC highlighting the effectiveness of the suggested EM strategy in maintaining superior PQ within hybrid MGs.

In addition to lowering the unit energy cost to 0.8 \$/Wh, the proposed strategy also contributes to long-term economic benefits. The reduction of power loss and THD decreases fuel consumption in diesel generators, while

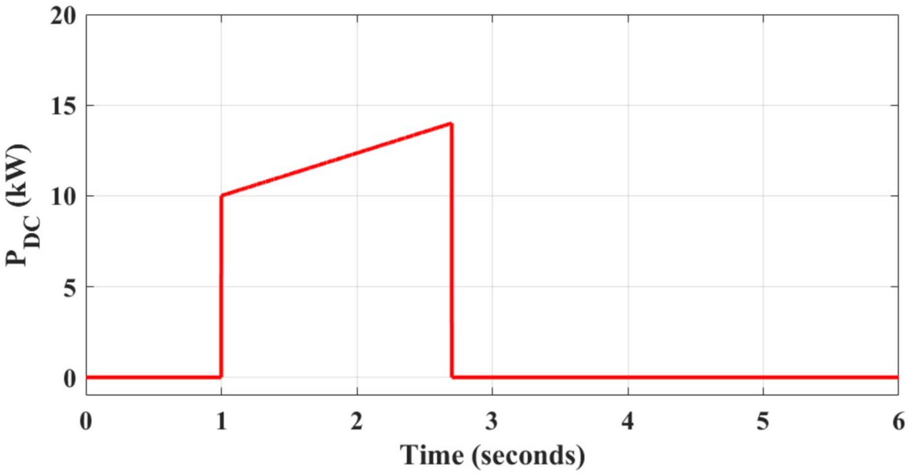

Fig. 15. Evaluation of diesel generator power.

Methods	Power loss (MW)	Efficiency (%)	Cost ($/Wh)	Execution time (sec)	THD (%)
ALA-TKAN	2.9	99.2	0.8	19	1.4
PDO-MACNN	3.4	98.2	1.1	25	2.1
BWO	4.3	97.3	1.4	31	3.4
PSO	5.1	96.4	1.5	29	2.9
ANN	5.6	95.7	1.9	35	3.8
MRA-FLC	4.0	97.8	1.2	22	2.7

Table 3. Performance comparison of suggested and existing approaches.

optimized HESS scheduling reduces charging/discharging stress, thereby extending battery and fuel cell lifetime. For a medium-scale hybrid microgrid (~ 100 kW), these improvements are expected to yield overall lifecycle cost savings of 12–15% compared to conventional EMS approaches. Moreover, the enhanced operational efficiency can shorten the payback period by approximately 2–3 years, making the proposed method more attractive for real-world deployment.

Discussion

The simulation results and comparative analysis clearly demonstrate the effectiveness of the suggested EM strategy for PQ improvement in hybrid MGs integrated with RESs and HESSs. The system exhibits stable and responsive behavior under varying conditions, as reflected in the dynamic profiles of various components. The power outputs of wind and PV stabilize at 10 kW and 6 kW respectively, ensuring a consistent renewable contribution. The DC-link voltage remains steady around 700 V with a step increase to 720 V, indicating reliable voltage regulation. The battery operates dynamically, charging around 4 kW and discharging at approximately −5 kW, adapting to fluctuations in demand. The load shows step changes from 25 to 20 kW and down to 15 kW, which the system successfully accommodates. The interlinking converter shifts from 3 to 6 kW and later to −2 kW, demonstrating its role in bidirectional power flow. Currents of both load and grid respond clearly to demand and disconnection events, maintaining waveform integrity. Voltage of the load remains stable at ± 325 V even after grid disconnection, confirming effective local voltage support, while the grid voltage and power drop to zero at 1 s and later recovers, showcasing seamless transition handling. The FC output holds steady at 28 kW, with only a brief dip, while the DG operates selectively, peaking at 14.5 kW, aligning generation with system needs. The comparative results reinforce these findings, with the suggested strategy achieving the lowest power loss of 2.9 MW, highest efficiency of 99.2%, minimum energy cost of 0.8 d$/Wh, shortest execution time of 19 s, and lowest THD of 1.4%. Together, these results confirm the robustness and superiority of the suggested approach in optimizing energy flow, enhancing PQ, and ensuring efficient, stable operation of hybrid MGS. To validate THD minimization, FFT-based harmonic analysis of load current and voltage was conducted. Prior to applying the ALA-TKAN approach, the harmonic spectrum exhibited significant low-order components, particularly the 5th and 7th harmonics, with an overall THD of approximately 3.8%. After applying ALA-TKAN, these harmonics were effectively suppressed, leading to a THD reduction to 1.4%. This confirms the method's capability to minimize harmonic distortion and improve PQ, aligning with IEEE-519 recommendations.

The superiority of the proposed ALA–TKAN framework over existing hybrid EM methods such as PDO–MACNN and ANN–PI controllers can be attributed to its integrated design. PDO–MACNN mainly addresses THD reduction and DC-link stability but lacks load forecasting and energy pricing considerations, while ANN–PI controllers stabilize voltage and manage SoC yet operate reactively without predictive scheduling. In contrast, ALA–TKAN establishes a unified framework where the Artificial Lemming Algorithm (ALA) optimizes power flow distribution and HESS operation, and the Temporal Kolmogorov–Arnold Network (TKAN) provides sequence-aware forecasting of load and renewable generation. This combination ensures proactive scheduling, faster convergence through adaptive exploration–exploitation strategies, and accurate temporal prediction of nonlinear system behaviors. As a result, ALA–TKAN consistently minimizes power loss (2.9 MW), THD (1.4%), and energy cost (0.8 \$/Wh), while achieving the highest efficiency (99.2%) and shortest execution time (19 s), thereby establishing a comprehensive improvement in PQ, stability, and system economics.

Deeper technical insights and scalability considerations

Beyond numerical improvements, the integration of ALA and TKAN provides several technical advantages. First, the forecasting capability of TKAN reduces the need for frequent re-optimization, since predicted demand and renewable profiles allow the optimizer to anticipate changes rather than reacting after disturbances occur. This synergy minimizes computational overhead while maintaining high accuracy in dynamic conditions. Second, the fast convergence of ALA (stabilizing within the first few iterations across multiple runs) directly translates to shorter execution times, which supports feasibility for near real-time energy management.

In terms of scalability, the proposed ALA–TKAN approach is inherently modular. Additional generation units, storage devices, or load clusters can be incorporated by expanding the decision variables handled by ALA and the input features fed into TKAN. Preliminary complexity analysis shows the framework scales approximately linearly with the number of decision variables ($O(N \times D \times T + L \times H^2 \times S)$), making it suitable for larger microgrids with dozens of distributed assets. Moreover, since TKAN can process parallel time-series inputs (e.g., PV, wind, load clusters), the forecasting component remains tractable for larger systems.

For real-time energy management system (EMS) deployment, the combined execution time of 19 s in the tested setup demonstrates practical feasibility, particularly for scheduling horizons in the order of minutes. Future work will focus on further reducing latency via lightweight TKAN architectures, implementing ALA in parallel computing environments, and validating the framework in hardware-in-the-loop simulations to confirm responsiveness under real operational constraints.

Computational complexity considerations

The computational complexity of the proposed ALA–TKAN framework can be expressed as $O(N \times D \times T + L \times H^2 \times S)$, where N is the number of search agents, D the decision variables, T the number of iterations, L the number of TKAN layers, H the hidden dimension, and S the forecast sequence length. The ALA component exhibits a similar order of complexity as conventional metaheuristics such as PSO or WOA but converges in fewer iterations due to its adaptive exploration–exploitation strategy. The TKAN component introduces only a modest additional cost relative to traditional ANN forecasting, while significantly improving prediction accuracy. Overall, simulation results confirmed that ALA–TKAN achieved the lowest execution time (19 s) compared to benchmark methods, thereby validating that the framework not only offers superior optimization accuracy but also maintains computational efficiency suitable for practical hybrid microgrid applications.

Conclusion

This manuscript presents an advanced EM strategy for enhancing PQ and operational efficiency in hybrid MGs integrating RESs and HESSs. The suggested method exhibits superior performance by effectively stabilizing voltage and frequency, minimizing power losses to 2.9 MW, achieving the highest energy efficiency of 99.2%, reducing energy cost to 0.8 \$/Wh, and maintaining the lowest THD at 1.4%. Compared to existing methods such as PDO–MACNN, BWO, PSO, ANN, and MRA–FLC, which exhibit higher power losses up to 5.6 MW, lower efficiencies down to 95.7%, higher energy costs up to 1.9 \$/Wh, and THD values reaching 3.8%, the suggested method consistently outperforms in all critical metrics. Simulation results further demonstrate its robust response to dynamic conditions, with stable power profiles across wind, PV, battery, converter, load, and generator systems. These outcomes validate the method's effectiveness in optimizing energy coordination, maintaining system reliability, and improving overall PQ, making it a strong solution for reliable and efficient hybrid MG operation.

Future works

Future research can extend the proposed strategy to large-scale microgrids with more complex load variations and higher renewable penetration. Emphasis may be placed on integrating real-time data analytics and enhanced forecasting models to support more adaptive energy management. Additional efforts could focus on strengthening system resilience under uncertainties, fault events, and communication delays. While the present study validates the ALA–TKAN method under steady-state and step-change load variations, further stress tests such as fault ride-through, rapid renewable intermittency, and transitions between islanded and grid-connected modes remain important for practical deployment. The predictive capability of TKAN and the optimization adaptability of ALA provide a strong foundation for addressing these challenges. Furthermore, hardware-in-the-loop (HIL) and real-time implementation studies will be pursued in future work to move toward experimental validation and practical feasibility of the proposed strategy.

Data availability

All data generated or analysed during this study are included in this published article.

Received: 21 August 2025; Accepted: 11 September 2025

References

1. Adeyinka, A. M., Esan, O. C., Ijaola, A. O. & Farayibi, P. K. Advancements in hybrid energy storage systems for enhancing renewable energy-to-grid integration. *Sustain. Energy Res.* **11**(1), 26 (2024).
2. Khosravi, N. Enhancing operational efficiency through a control-based approach for hydrogen and battery energy storage systems integration in renewable energy networks. *Renew. Energy.* **248**, 123132 (2025).
3. Abdelghany, M. B., Al-Durra, A. & Gao, F. A coordinated optimal operation of a grid-connected wind-solar microgrid incorporating hybrid energy storage management systems. *IEEE Trans. Sustain. Energy* **15**(1), 39–51 (2023).
4. Jena, C. J., Ray, P. K., Panda, G. & Nandkeolyar, S. Power Quality Enhancement and Power Management of PV-HESS based Grid-tied Microgrid using Model Predictive Control Approach. *IEEE Trans. Ind. Appl.* https://doi.org/10.1109/TIA.2024.3523876 (2024).
5. SadolaluBoregowda, V. K. et al. Enhancing DC microgrid performance with fuzzy logic control for hybrid energy storage system. *SIViP* **18**(5), 4505–4514 (2024).
6. Upadhayay, T. & Jamnani, J. Integrating Hybrid Energy Storage System for Power Quality Enhancement of Grid Integrated Large Scale Wind Energy System. *Smart Grids and Sustainable Energy* **10**(1), 1 (2024).
7. Aghmadi, A., Ali, O. & Mohammed, O. A. Stability Enhancement of DC Microgrid Operation Involving Hybrid Energy Storage and Pulsed Loads. *IEEE Trans. Consum. Electr.* https://doi.org/10.1109/TCE.2025.3545309 (2025).
8. Panda, M., Chankaya, M., Mohanty, S. & Sandeep, S. D. State-of-charge based energy management strategy for hybrid energy storage system in DC microgrid. *IEEE Access* https://doi.org/10.1109/ACCESS.2025.3564786 (2025).
9. Patel, S., Ghosh, A., Ray, P. K. & Gurugubelli, V. Effective power management strategy and control of a hybrid microgrid with hybrid energy storage systems. *IEEE Trans. Ind. Appl.* **59**(6), 7341–7355 (2023).
10. Behera, P. K. & Pattnaik, M. Hybrid energy storage integrated wind energy fed DC Microgrid power distribution control and performance assessment. *IEEE Trans. Sustain. Energy* **15**(3), 1502–1514 (2024).
11. Seedahmed, M. M., Ramli, M. A., Abusorrah, A. & Alqahtani, M. M. Control-oriented model of an optimally designed hybrid storage system for a standalone microgrid. *IEEE Access* **11**, 119161–119186 (2023).
12. Al-Khayyat, A. S., Hameed, M. J. & Ridha, A. A. Optimized power flow control for PV with hybrid energy storage system HESS in low voltage DC microgrid. *E - Prime – Adv. Electr. Eng. Electr. Energy* **6**, 100388 (2023).
13. Moghadam, M. & Ghaffarzadeh, N. Suppressing solar PV output fluctuations by designing an efficient hybrid energy storage system controller. *Unconv. Resour.* **4**, 100077 (2024).
14. Yang, Y. et al. A hierarchical energy management strategy for DC microgrid hybrid energy storage systems based on fractional-order sliding mode controller. *J. Energy Storage* **99**, 113307 (2024).
15. Ranjan, M. & Shankar, R. Improved frequency regulation in smart grid system integrating renewable sources and hybrid energy storage system. *Soft. Comput.* **28**(11), 7481–7500 (2024).
16. Krishnakumar, R. et al. Energy management of energy hub with renewable energy resources based on GTOA-ACNN approach. *Environ. Develop. Sustain.* https://doi.org/10.1007/s10668-025-06239-8 (2025).
17. Bhoopathi, M. et al. PV Fed Grid System with PI Controller for Enhancing Power Quality Using CMBO-PCSANN Approach. *IETE J. Res.* https://doi.org/10.1080/03772063.2025.2469639 (2025).
18. Rangasamy, S., Arun Prakash, S., Sakhare, N. N. & Arun Kumar, U. Multiple microgrids with electric vehicle charging in a hybrid GJO-PCGAN approach for energy management. *Electr. Eng.* https://doi.org/10.1007/s00202-024-02922-7 (2025).
19. Lakshmiprabha, K. E. et al. Efficiency and economic assessment of wind turbine-powered pumped hydro-compressed air storage coupled with alkaline fuel cell using hybrid approach. *Clean Technol. Environ. Policy* **26**(12), 4255–4272 (2024).
20. Sakthivel, A. et al. Enhancing electric vehicle performance through buck-boost converters with renewable energy integration using hybrid approach. *Optim. Control Appl. Methods* **45**(5), 2231–2252 (2024).
21. Vennila, C., Papana, V. P., Reddy, C. V. K. & Kumar, U. A. ALSO-DCGNN : enhancing power quality and voltage regulation of energy storage systems in DC micro grid. *Environ. Develop. Sustain.* https://doi.org/10.1007/s10668-024-05226-9 (2024).
22. Bhoopathi, M. et al. Unbalanced operation of integrated power distribution system for optimal energy flow using LSO-vCANNs approach. *Environ. Develop. Sustain.* https://doi.org/10.1007/s10668-024-05121-3 (2024).
23. Varghese, L. J., Arun Kumar, U. & Sunitha, D. Solar PV and wind energy based reconfigurable microgrid for optimal load dispatch. *J. Electr. Eng. Technol.* **18**(4), 2909–2928 (2023).
24. Sathishkumar, R., Venkateswaran, M., Deepamangai, P. & SoundarRajan, P. An efficient power management control strategy for grid-independent hybrid renewable energy systems with hybrid energy storage: Hybrid approach. *J. Energy Storage* **96**, 112685 (2024).
25. Alharbi, A. G., Olabi, A. G., Rezk, H., Fathy, A. & Abdelkareem, M. A. Optimized energy management and control strategy of photovoltaic/PEM fuel cell/batteries/supercapacitors DC microgrid system. *Energy* **290**, 130121 (2024).
26. Abu, S. M. et al. An effective optimization algorithm for hydrogen fuel cell-based hybrid energy system: A sustainable microgrid approach. *Int. J. Hydrog. Energy.* **98**, 1341–1355 (2025).
27. Ramu, S. K., Vairavasundaram, I., Palaniyappan, B., Bragadeshwaran, A. & Aljafari, B. Enhanced energy management of DC microgrid: Artificial neural networks-driven hybrid energy storage system with integration of bidirectional DC-DC converter. *J. Energy Storage* **88**, 111562 (2024).
28. Rajput, A. K. & Lather, J. S. Energy management of a DC microgrid with hybrid energy storage system using PI and ANN based hybrid controller. *Int. J. Ambient Energy* **44**(1), 703–718 (2023).
29. Sruthi, S., Karthikumar, K. & Chandrasekhar, P. An efficient power management control strategy for grid-independent hybrid renewable energy systems with hybrid energy storage: Hybrid approach. *Journal of Energy Storage* **95**, 112325 (2024).
30. Chekira, O. et al. An improved microgrid energy management system based on hybrid energy storage system using ANN NARMA-L2 controller. *J. Energy Storage* **98**, 113096 (2024).
31. Firah, A., Birane, M., Degla, A. & Hadroug, N. Energy Management and Improved Metaheuristic Optimization-Based Control of Photovoltaic/Hybrid Energy Storage System-Based Microgrid. *Arabian J. Sci. Eng.* https://doi.org/10.1007/s13369-025-10072-6 (2025).
32. Mahjoub, S., Chrifi-Alaoui, L., Drid, S. & Derbel, N. Control and implementation of an energy management strategy for a PV–wind–battery microgrid based on an intelligent prediction algorithm of energy production. *Energies* **16**(4), 1883 (2023).
33. Rausell, E., Arnaltes, S., Rodríguez, J. L., Lafoz, M. & Navarro, G. Control of wind energy conversion systems with permanent magnet synchronous generator for isolated green hydrogen production. *Int. J. Hydrogen Energy* **107**, 241–251 (2025).
34. Long, Q., Yu, H., Xie, F., Lu, N. & Lubkeman, D. Diesel generator model parameterization for microgrid simulation using hybrid box-constrained levenberg-marquardt algorithm. *IEEE Trans. Smart Grid* **12**(2), 943–952 (2020).
35. Abdelkader, A. B., Mouloudi, Y. & Soumeur, M. A. Integration of renewable energy sources in the dynamic voltage restorer for improving power quality using ANFIS controller. *J. King Saud Univ. Eng. Sc.* **35**(8), 539–548 (2023).
36. Sun, B. A multi-objective optimization model for fast electric vehicle charging stations with wind, PV power and energy storage. *J. Clean. Prod.* **288**, 125564 (2021).
37. Xiao, Y., Cui, H., Khurma, R. A. & Castillo, P. A. Artificial lemming algorithm: a novel bionic meta-heuristic technique for solving real-world engineering optimization problems. *Artif. Intell. Rev.* **58**(3), 84 (2025).
38. Genet, R., & Inzirillo, H. Tkan: Temporal kolmogorov-arnold networks. Preprint at arXiv:2405.07344 (2024).

Acknowledgements

This article has been produced with the financial support of the European Union under the REFRESH—Research Excellence For Region Sustainability and High-tech Industries project number CZ.10.03.01/00/22_003/0000048 via the Operational Programme Just Transition.

Author contributions

J.S and A.F: Conceptualization, Methodology, Software, Investigation, Data Validation and Writing—Original draft preparation; K.M and S.C: Supervision, Resources, Data Validation, Visualization, Data Curation, Writing—Reviewing and Editing.

Funding

This article has been produced with the financial support of the European Union under the REFRESH—Research Excellence For Region Sustainability and High-tech Industries project number CZ.10.03.01/00/22_003/0000048 via the Operational Programme Just Transition.

Declarations

Competing interests

The authors declare no competing interests.

Additional information

Correspondence and requests for materials should be addressed to S.J.D. or A.F.

Reprints and permissions information is available at www.nature.com/reprints.

Publisher's note Springer Nature remains neutral with regard to jurisdictional claims in published maps and institutional affiliations.

Open Access This article is licensed under a Creative Commons Attribution-NonCommercial-NoDerivatives 4.0 International License, which permits any non-commercial use, sharing, distribution and reproduction in any medium or format, as long as you give appropriate credit to the original author(s) and the source, provide a link to the Creative Commons licence, and indicate if you modified the licensed material. You do not have permission under this licence to share adapted material derived from this article or parts of it. The images or other third party material in this article are included in the article's Creative Commons licence, unless indicated otherwise in a credit line to the material. If material is not included in the article's Creative Commons licence and your intended use is not permitted by statutory regulation or exceeds the permitted use, you will need to obtain permission directly from the copyright holder. To view a copy of this licence, visit http://creativecommons.org/licenses/by-nc-nd/4.0/.

© The Author(s) 2025